ACS APPLIED MATERIALS & INTERFACES

www.acsami.org

Research Article

A CuNi Alloy–Carbon Layer Core–Shell Catalyst for Highly Efficient Conversion of Aqueous Formaldehyde to Hydrogen at Room Temperature

Zining Zhou, Yun Hau Ng, Shengju Xu, Siyuan Yang, Qiongzhi Gao, Xin Cai,* Jihai Liao,* Yueping Fang, and Shengsen Zhang*

Cite This: *ACS Appl. Mater. Interfaces* 2021, 13, 37299–37307

Read Online

ACCESS | Metrics & More | Article Recommendations | Supporting Information

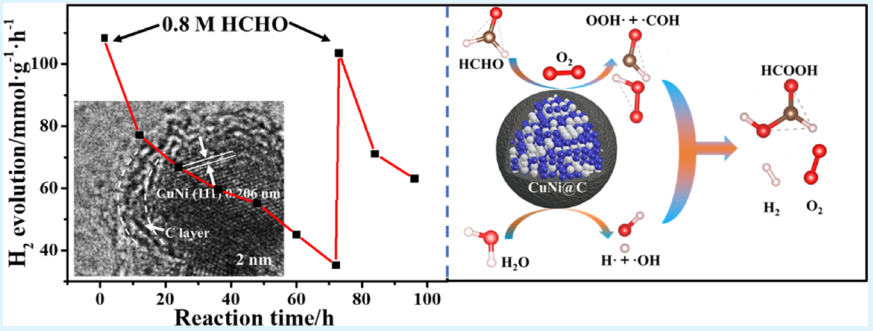

ABSTRACT: A copper (Cu) material is catalytically active for formaldehyde (HCHO) dehydrogenation to produce H_2, but the unsatisfactory efficiency and easy corrosion hinder its practical application. Alloying with other metals and coating a carbon layer outside are recognized as effective strategies to improve the catalytic activity and the long-term durability of nonprecious metal catalysts. Here, highly dispersed CuNi alloy–carbon layer core–shell nanoparticles (CuNi@C) have been developed as a robust catalyst for efficient H_2 generation from HCHO aqueous solution at room temperature. Under the optimized reaction conditions, the CuNi@C catalyst exhibits a H_2 evolution rate of 110.98 mmol·h^{-1}·g^{-1}, which is 1.5 and 4.9 times higher than those of Cu@C and Ni@C, respectively, which ranks top among the reported nonprecious metal catalysts for catalytic HCHO reforming at room temperature to date. Furthermore, CuNi@C also displays excellent stability toward the catalytic HCHO reforming into H_2 in tap water owing to the well-constructed carbon sheath protecting CuNi nanocrystals from oxidation in an alkaline medium. Combined with density functional theory calculations, the superior catalytic efficiency of CuNi@C for H_2 generation results from the synergistic contribution between the massive active species from HCHO decomposition on the Cu sites and the remarkable H_2 evolution activity on Ni sites. The improved performance of CuNi@C highlights the enormous potential of advancing noble-metal-free nanoalloys as cost-effective and recyclable catalysts for energy recovery from industrial HCHO wastewater.

KEYWORDS: *dehydrogenation, formaldehyde, CuNi alloy catalyst, carbon layer, hydrogen generation*

1. INTRODUCTION

Hydrogen (H_2), as a clean energy source with ultrahigh specific energy density, has incomparable prospects of replacing fossil fuels, while the two major obstacles of transportation and safe storage limit its large-scale application.[1,2] An alternative approach is to release H_2 from a chemically stable liquid, ideally encompassing hydrogen-rich aqueous biomass-derived resources.[3] To this end, inexpensive formaldehyde (HCHO) is a desirable medium for H_2 storage and transportation as it can be reformed with water to release H_2 at a high theoretical weight density of 8.4%.[4] Since the 1990s, noble-metal-based nanomaterials, such as Pd,[5,6] Ag,[7] Pt,[8] Au,[9] and Ru complexes,[10−12] have been used for catalyzing HCHO reforming to produce H_2. Such noble-metal catalysts exhibit high catalytic activity and long-term stability. Moreover, little undesired substances are generated during the reaction, thereby intriguing continuous interest for H_2 generation from HCHO solution. Nonetheless, the drawbacks of low natural reserves, high cost, and difficult recovery seriously restrict their practical use in industrial generation.[13,14] In this regard, increasing attention has been paid to developing nonprecious

Received: June 23, 2021
Accepted: July 19, 2021
Published: July 29, 2021

https://doi.org/10.1021/acsami.1c11776
ACS Appl. Mater. Interfaces 2021, 13, 37299–37307

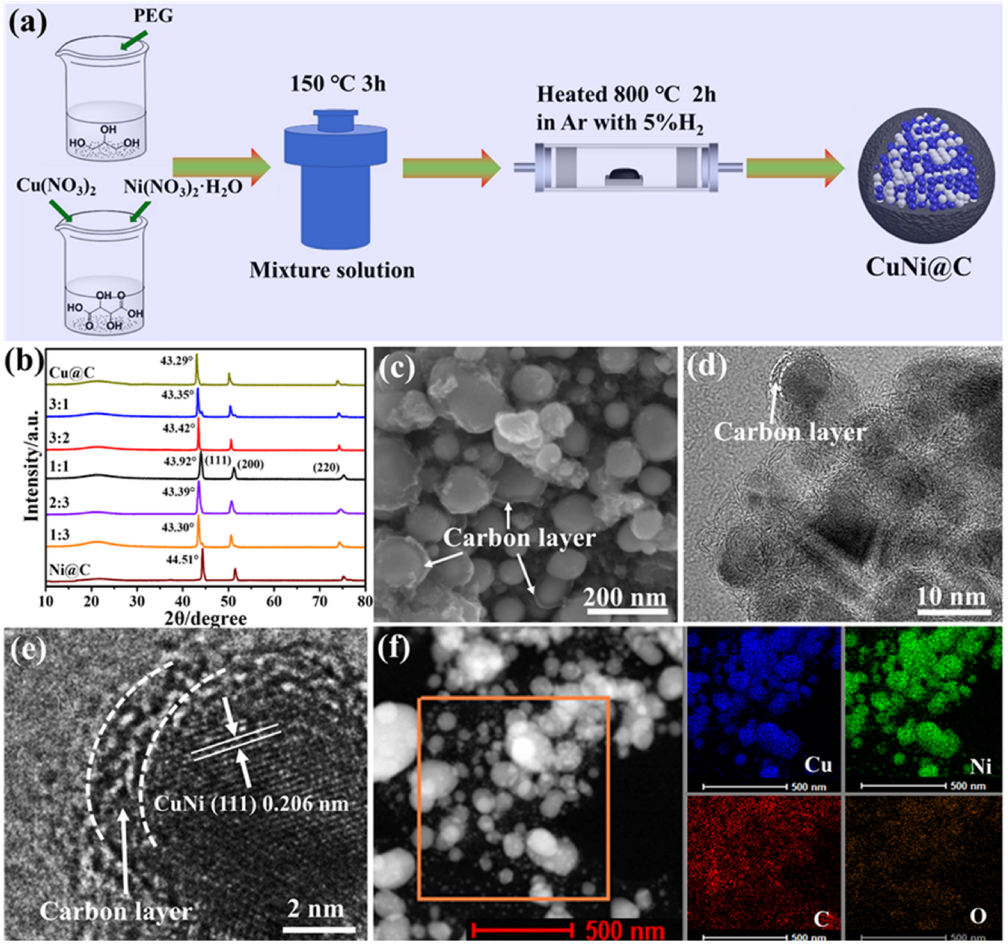

Figure 1. (a) Schematic illustrations of the synthesis processes of CuNi@C; (b) XRD patterns of CuNi@C samples prepared with different Cu/Ni ratios; (c) SEM image, (d,e) TEM images, and (f) TEM-EDX element mapping images of $CN_{(1:1)}$.

metal catalysts, such as Cu,[15−19] MnO_2,[20] V_2O_5,[21] WO_2,[22] and so on.

Among numerous noble-metal-free catalysts, Cu-based nanocatalysts are the most attractive candidates and widely studied for electrochemical reduction,[23,24] solar-to-hydrogen evolution,[25,26] and environmental catalysis.[27,28] They are also used to catalytically reform HCHO for H_2 generation due to their high specific surface area, macroscopic quantum tunneling effect, and superb activities.[15−19] However, these works are mainly focused on nano-Cu, Cu_2O, and their complexes, which belong to the single-phase catalyst, and the efficiency needs to be further improved. What is more, Cu or Cu_2O nanocatalysts still suffer from low efficiency and severe corrosion/degradation in the alkaline solution.[29,30] Therefore, it is of great significance to exploit more efficient Cu-based catalysts with enhanced utilization efficiency.

Recently, the high catalytic performance of noble-metal-free alloys has attracted much attention due to their interplay of electronic and lattice effects among the neighboring metal atoms.[31−34] Noble-metal-free alloys have been widely used as catalysts for oxygen reduction reaction (Cr−Mn−Fe−Co−Ni[35] and FeCoNi[36]), hydrogen evolution reaction (NiCu/CeO_2[32] and CuNi@C═O[34]), and chemical hydrogen storage (FeNi alloy[33] and FeNi/CeO_2[31]). Enlightened by synergistic effects of neighboring metals, we believe that a suitable noble-metal-free alloy is likely to have the ability to catalyze HCHO dehydrogenation for effective H_2 evolution. Metallic Ni has been identified as an alternative catalyst to produce H_2.[37,38] Technically, combining Cu with Ni to form a CuNi alloy with an elaborated nanostructure and sufficiently exposed surface active sites is expected to display highly improved catalytic H_2 generation from HCHO and H_2O. Regarding the stability of the catalysts, proper carbon layer coating is a promising approach owing to its unique benefits covering excellent mechanical strength, superior chemical tolerance, and diversified composition design. In general, the carbon layer can dramatically improve the chemical stability and assist the catalytic kinetics of nonprecious metal catalysts.[37,39] Therefore, it would be of great significance to develop well-defined carbon-coated CuNi alloy nanocatalysts for boosting H_2 evolution from HCHO aqueous reforming.

Here, CuNi alloy−carbon layer core−shell nanoparticles (CuNi@C) are prepared via one-step synthesis and for the first time used as a catalyst for producing H_2 from HCHO solution at room temperature. Specifically, the effects of the Cu−Ni atomic ratio in CuNi@C and the reaction conditions on the catalytic H_2 generation performance are elucidated. Under the optimal conditions, the initial H_2 generation rate of the CuNi@C catalyst is almost the highest efficiency of nonprecious metal catalysts for catalytic HCHO reforming at room temperature. Furthermore, the high catalytic activity of CuNi@C can still be maintained in tap water-simulated industrial HCHO wastewater. Combined with the experimental results,

https://doi.org/10.1021/acsami.1c11776
ACS Appl. Mater. Interfaces 2021, 13, 37299−37307

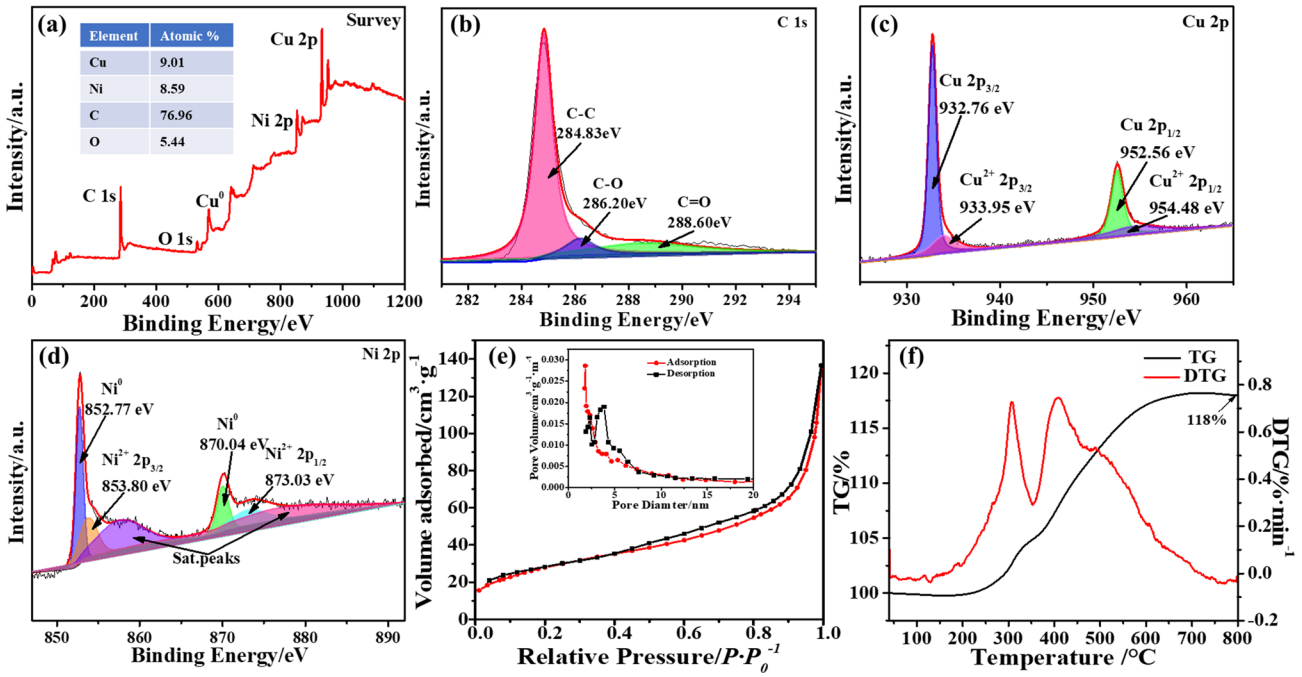

Figure 2. (a) Survey, (b) C 1s, (c) Cu 2p, and (d) Ni 2p XPS spectra of the $CN_{(1:1)}$ sample; (e) BET and (f) TG analysis of the $CN_{(1:1)}$ sample.

the mechanism of the catalytic reaction is explored by density functional theory (DFT) calculations.

2. EXPERIMENTAL SECTION

2.1. Preparation of the CuNi@C Catalyst. CuNi@C was prepared by a one-step synthesis method (Figure 1a). Typically, 755 mg of $Cu(NO_3)_2{\cdot}3H_2O$, 908 mg of $Ni(NO_3)_2{\cdot}6H_2O$, and 1876 mg of tartaric acid ($C_4H_6O_6$) were added to 20 mL of deionized water and stirred to dissolve. The obtained solution was then mixed with another solution consisting of 5 g of polyethylene glycol, 48 mL of glycerol, and 12 mL of deionized water. The mixed solution was transferred to a Teflon-lined stainless-steel autoclave and heated to 150 °C for 3 h. A solid product was obtained after centrifugation, alcohol washing, and drying at 60 °C for 24 h. After that, the resulting solids were calcined at 800 °C for 2 h with a heating rate of 3 °C·min^{-1} under Ar with 5% H_2 protection. The obtained material was CuNi@C nanoparticles whose molar ratio of Cu to Ni was 1:1 and denoted as $CN_{(1:1)}$. Other samples of $CN_{(1:3)}$, $CN_{(2:3)}$, $CN_{(3:2)}$, $CN_{(3:1)}$, Cu@C, and Ni@C were prepared by changing the ratio of $Cu(NO_3)_2{\cdot}3H_2O$ and $Ni(NO_3)_2{\cdot}6H_2O$.

2.2. Characterizations. The morphology of the CuNi@C samples was observed by scanning electron microscopy (SEM, Quanta 200 FEG, FEI, America) and transmission electron microscopy (TEM, Glacios Cryo-TEM, Thermo Fisher Scientific, America). The phase structure of CN was determined by X-ray diffraction (XRD, Ultima IV, RIGAKU, Japan). The surface chemical properties were determined by X-ray photoelectron spectroscopy (XPS, VG ESCALAB 250, Thermo VG Scientific, America). The Brunauer–Emmett–Teller (BET) specific surface area (S_{bet}) and the surface structure were analyzed from nitrogen adsorption/desorption isotherms using a specific surface and porosity analyzer (Gemini-2390, Micromeritics, America). The carbon content was analyzed using a DTA/TGA analyzer (TG, DTG-60, Shimadzu, Japan). The reaction mechanism was analyzed by electron paramagnetic resonance (EPR) tests using an electron paramagnetic resonance spectrometer (JES FA200, JEOL, Japan). Hydrogen evolution reaction (HER) tests were used to characterize the hydrogen evolution performance of the sample by using an electrochemical workstation (Chi 650e, Shanghai Chenhua, China), and the test method followed our previous work.[34]

2.3. Catalytic H_2 Evolution Measurements. Ten milligrams of the catalyst was added into a glass beaker containing 100 mL of aqueous solutions of KOH and HCHO. The suspension was transferred to a sealed quartz reactor with an air atmosphere for reaction under strong agitation (1200 rpm). The catalytic activity of the samples was compared by measuring the H_2 yield by gas chromatography (GC-7900, Shanghai Tianmei Scientific Instrument Co., Ltd., China). The influence of each reaction condition on the reaction performance of the catalyst was investigated by controlling variables.

2.4. Computational Methods. All of the geometries and energy were calculated by employing density functional theory (DFT) as implemented in the Vienna ab initio simulation package (VASP). The theoretical model of CuNi@C was constructed by XRD, XPS, EDX, and other characterization results, and DFT calculation and nudged elastic band (NEB) calculation of the reaction process of different active sites were carried out. The mechanism of the reaction was further explained by combining the calculation results with the experimental results. The specific parameters and models used in the calculation can be found in the Supporting Information.

3. RESULTS AND DISCUSSION

3.1. Characterization. The XRD patterns in Figure 1b show that the diffraction peaks at 44.51, 51.85, and 76.37° on Ni@C correspond to the (111), (200), and (220) planes of the Ni crystal (JCPDS no. 04-0850), indicating the formation of Ni nanoparticles. Meanwhile, the peaks at 43.29, 50.43, and 74.13° on Cu@C are ascribed to the (111), (200), and (220) planes of the Cu crystal (JCPDS no. 04-0836), indicating the formation of Cu nanoparticles. The peaks of the CN samples are all located between the diffraction peaks of Cu and Ni, confirming the formation of the CuNi alloy. For example, the peaks of $CN_{(1:1)}$ at 2θ of 43.94, 51.19, and 75.32° represent the diffractions of the (111), (200), and (220) planes of the CuNi alloy (JCPDS no. 65-9048), respectively. By comparing the characteristic peaks of the five CN samples, the positions of the peaks are slightly different, which can be attributed to the change of the crystal plane distance caused by the different molar ratios of Cu/Ni. The peak values of $CN_{(3:1)}$ at 43.35° and $CN_{(1:3)}$ at 43.30° obviously shift from that of the CuNi alloy (43.92°), which can be attributed to the formation of a

https://doi.org/10.1021/acsami.1c11776
ACS Appl. Mater. Interfaces 2021, 13, 37299−37307

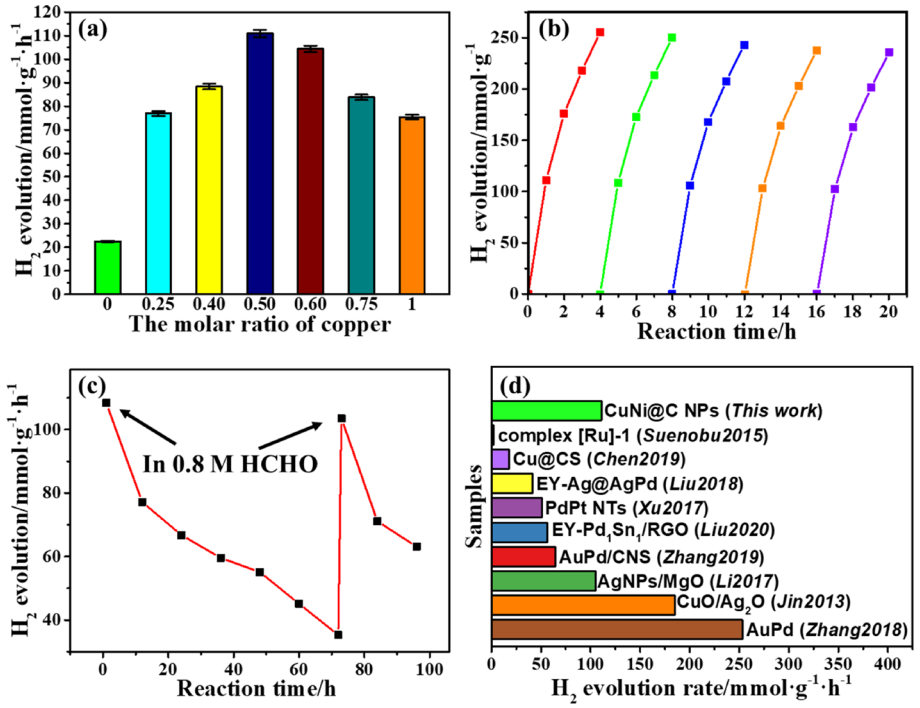

Figure 3. Influence of (a) Cu−Ni atomic ratio in CN samples; (b) reusability of $CN_{(1:1)}$ for H_2 generation and (c) long-term stability of the catalyst in a tap water system of the $CN_{(1:1)}$ sample (0.8 M HCHO, 1 M NaOH, and 0.21 atm of O_2); (d) maximum H_2 generation rate compared with reported works.

segregated Ni phase. These results reveal that an equimolar ratio between Cu and Ni atoms facilitates the formation of a CuNi alloy. In addition, a broad peak at 21.17° for each sample is attributed to carbon.

The SEM image of the $CN_{(1:1)}$ sample (Figure 1c) shows nanoparticles with a size of 40−100 nm and a thin carbon layer outside each nanoparticle (see the arrows). The TEM images of the $CN_{(1:1)}$ catalyst (Figure 1d,e) show the apparent carbon layer structure and the (111) crystal plane of CuNi with a lattice fringe of 0.206 nm. Regular crystal planes and carbon-coated structures can also be found in the TEM images of Ni@C and Cu@C (Figure S1), indicating the formation of carbon-coated nanometals. TEM-EDX element mapping images of the $CN_{(1:1)}$ sample (Figure 1f) reveal the presence of Cu, Ni, C, and O elements. The Cu and Ni images show high density and a complete overlap in the interior of the particles, indicating the formation of CuNi alloy nanoparticles. These results demonstrate that a nano-CuNi alloy wrapped with a thin carbon layer has been prepared.

The XPS survey spectra (Figure 2a) also reveal the presence of C, Cu, Ni, and O elements in $CN_{(1:1)}$. Due to the coating of a carbon layer, most of the Cu and Ni are not detected, but the existence of Cu−Ni atoms with an equal ratio can still be found. The at. % of O is much less than that of C, proving that the content of O is very low, indicating that the content of the oxygen element is controlled in a low range by hydrogen reduction. The high-resolution XPS spectrum of C 1s with three peaks at 284.83, 286.20, and 288.60 eV is deconvoluted (Figure 2b), which corresponds to the C−C/C═C, C−O, and C═O species, respectively.[40−42] Figure 2c shows the Cu $2p_{3/2}$ and Cu $2p_{1/2}$ peaks. The Cu $2p_{3/2}$ peak could be deconvoluted into two peaks centered at 932.76 and 933.95 eV, which may be attributed to Cu^0 (or Cu^+) and Cu^{2+}, respectively. The peak−peak difference between Cu $2p_{3/2}$ (932.76 eV) and Cu $2p_{1/2}$ (952.56 eV) is 20.80 eV, also revealing the presence of Cu^0 (agreeing well with the result from XRD).[43] The Ni 2p peak in Figure 2d is deconvoluted into six peaks, and two of them are satellite peaks, being consistent with the literature reports for the existence of metallic Ni and Ni^{2+}.[44−46] The existence of Cu^+, Cu^{2+}, and Ni^{2+} can be attributed to the slightly oxidized surface of the CuNi alloy. To sum up, XPS analysis shows that Cu and Ni mainly exist in the form of Cu^0 and Ni^0, and they have no obvious chemical interaction with carbon.

The nitrogen adsorption−desorption isotherms of the $CN_{(1:1)}$ sample in Figure 2e exhibit an apparent hysteresis loop between the relative pressures of 0.1 and 1. The curve is a type-IV model adsorption/desorption isotherm, indicative of the mesoporous structure of the catalyst. Furthermore, the type of the hysteresis ring is an H3 type, indicating that slit holes are formed by particle accumulation in the material.[47] The average pore size of the material is 9.2 nm by Barrett−Joyner−Halenda (BJH) model analysis (inset in Figure 2e), which further provides evidence for the mesoporous properties of the material. These results show that most of the pore volume and specific surface area are provided by mesopores, and a developed pore structure has been formed. According to the BET linear curve fitting, the specific surface area of the material is 101 $m^2 \cdot g^{-1}$, while the Langmuir specific surface area is 163.6 $m^2 \cdot g^{-1}$, displaying that the alloy material has a large specific surface area and suggesting that it has numerous active sites.

TG analysis of $CN_{(1:1)}$ was carried out in air at a heating rate of 10 °C min^{-1}, as shown in Figure 2f. As the temperature rises from 200 to 700 °C, the mass of the material continues to increase due to the oxidation of the metal CuNi alloy in air. When the temperature is between 300 and 400 °C, the rising rate of the material mass decreases obviously, which is caused by the oxidation loss of the outer carbon layer. When the

https://doi.org/10.1021/acsami.1c11776
ACS Appl. Mater. Interfaces 2021, 13, 37299−37307

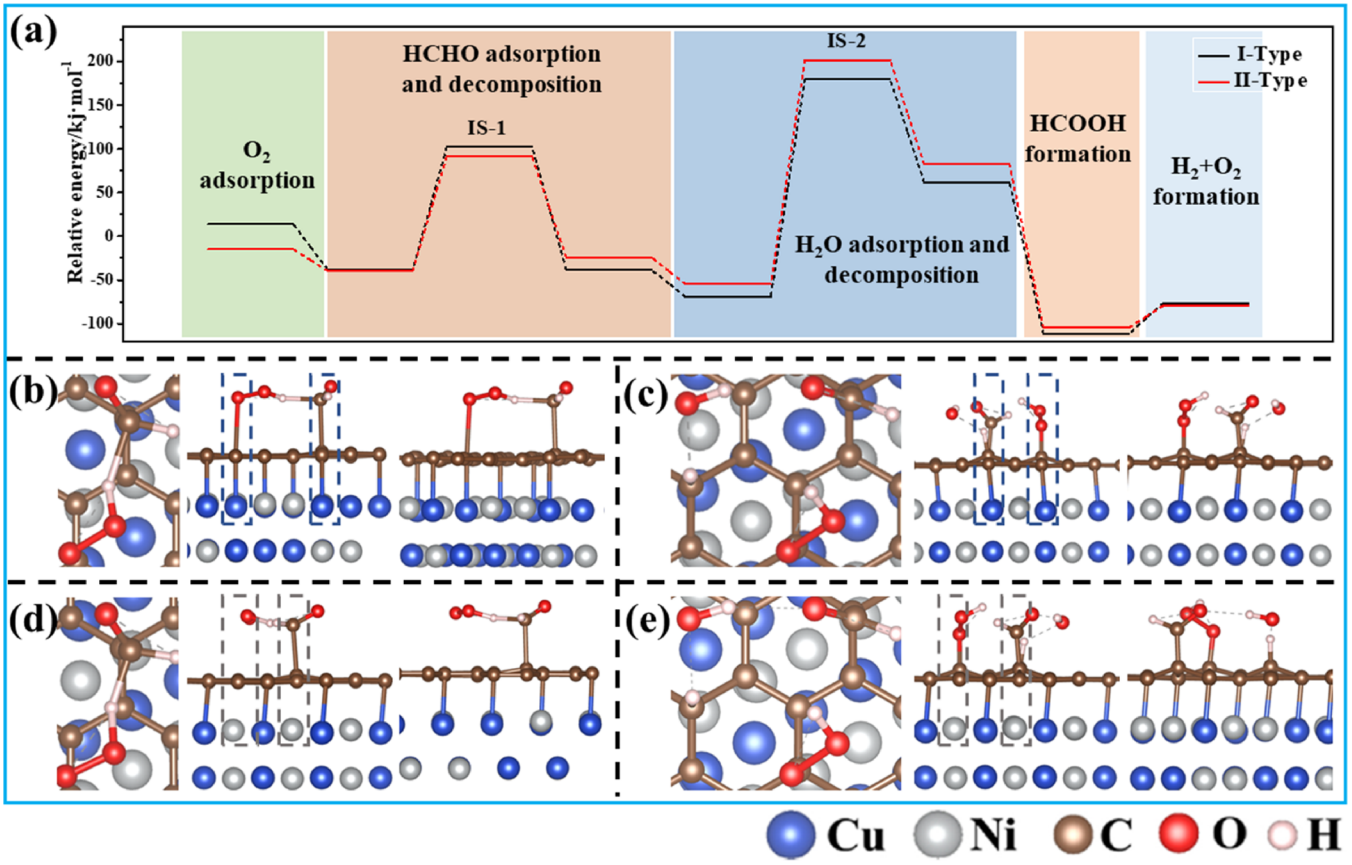

Figure 4. (a) DFT calculation results; IS-1 process (b) and IS-2 process (c) of the I-type; IS-1 process (d) and IS-2 process (e) of the II-type.

temperature is increased to 800 °C, the mass of the material is 118% of the initial sample, and it does not change anymore. At this time, the carbon layer is completely lost, the Cu−Ni alloy is completely oxidized to CuO and NiO, and their molar ratio is 1:1. According to these data, it can be inferred that the content of the CuNi metal in the $CN_{(1:1)}$ sample is 93.6%. In addition, the water content can be concluded from Figure 2f to be 1%, calculating that the carbon content in the sample is about 5.4%. These results display that the catalyst is made of the Cu−Ni alloy and carbon, consistent with the physical characterizations aforementioned.

3.2. Catalytic Performances. The influences of the initial KOH concentration, HCHO concentration, and O_2 concentration in the reaction system on hydrogen generation performance were studied systematically. Figure S2 displays that the optimal condition is 10 mg of the catalyst, 1.0 M KOH, 0.8 M HCHO, a higher O_2 partial pressure, and a higher reaction temperature. Considering economy and practicality, subsequent experiments were carried out in an air atmosphere and temperature, i.e., 0.21 atm of O_2 and 25 °C.

To investigate the effect of the Cu−Ni atomic ratio in the CuNi@C catalyst, the rates of H_2 generation over Cu@C, Ni@C, and different CuNi@C catalysts for HCHO dehydrogenation under 1 M KOH and 0.21 atm O_2 conditions were tested. It is found that the sample of $CN_{(1:1)}$ with a 1:1 Cu−Ni atomic ratio has the highest H_2 generation rate of 110.98 $mmol \cdot g^{-1} \cdot h^{-1}$ (Figure 3a), 1.47 times and 4.93 times higher than those of Cu@C (75.40 $mmol \cdot g^{-1} \cdot h^{-1}$) and Ni@C (22.50 $mmol \cdot g^{-1} \cdot h^{-1}$), respectively. The results show that all the CuNi alloys have better HCHO dehydrogenation than the single-metal catalyst. In the following studies, we focus on the best sample of $CN_{(1:1)}$.

To evaluate the cyclic stability of the catalyst, 10 mg of $CN_{(1:1)}$ was taken for H_2 generation reaction for 4 h under the optimized conditions, and then, the sample was recovered by centrifugal operation for further use for a H_2 generation test again. Figure 3b shows that the H_2 generation experiment is repeated for 5 cycles, and the H_2 generation efficiency remains 92% of that of the first experiment. To investigate the feasibility of the CuNi@C catalyst in practical application, a long-term (100 h) catalytic test was carried out in a system of tap water as a solvent for HCHO (Figure 3c). At the beginning of the reaction, the catalyst has a high catalytic efficiency, and tap water has little effect on the efficiency of the catalyst. As the reaction proceeds, the rate of H_2 generation decreases gradually. After formalin is added to make the concentration back to the initial HCHO concentration, the reaction rate increases dramatically and close to that of the first hour, indicating that the decrease in the H_2 generation rate is due to the depletion of HCHO. The XRD pattern and the TEM image of the recovered sample are shown in Figure S3, which is almost the same as the sample structure before the reaction. These results suggest that the nano-CuNi@C is an efficient catalyst with extremely high long-term catalytic stability for H_2 generation in HCHO solution. Compared with the previously reported performance (Figure 3d),[6,17,48−50] the $CN_{(1:1)}$ catalyst in this work has an excellent H_2 generation from HCHO solution among the non-noble-metal catalysts, even higher than those of some noble-metal catalysts.

3.3. Density Functional Theory (DFT) Calculations. DFT calculations are usually used to explore the catalytic

https://doi.org/10.1021/acsami.1c11776
ACS Appl. Mater. Interfaces 2021, 13, 37299−37307

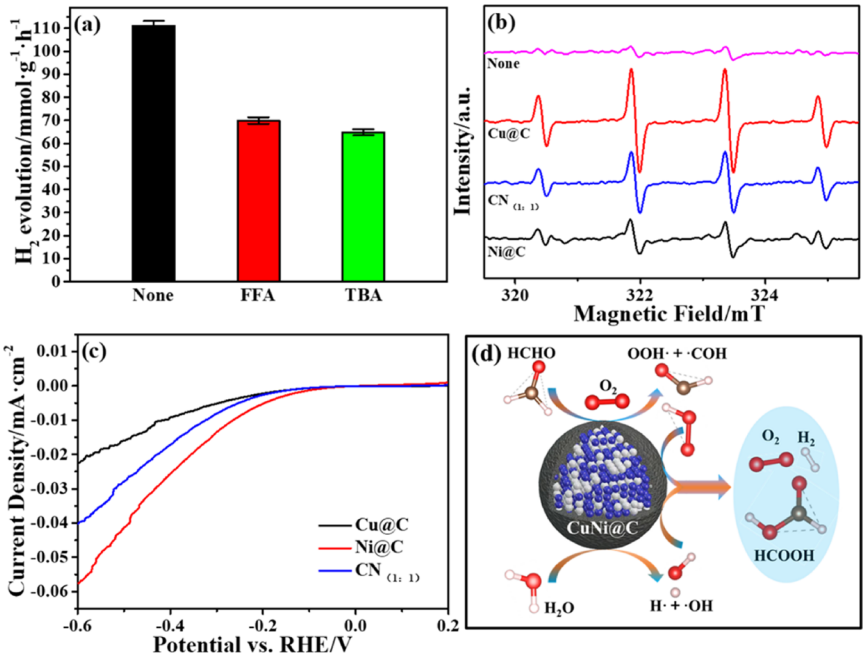

Figure 5. (a) Free-radical quenching experiment; (b) EPR test of different samples under the same reaction conditions; (c) HER test of Cu@C, Ni@C, and $CN_{(1:1)}$; (d) catalytic schematic diagram of CuNi@C for H_2 generation in HCHO solution.

reaction mechanism from the theoretical level. In this work, catalyst models were constructed to provide detailed information about the energetics and structure of the elemental reaction steps. The model was based on an alloy phase with a Cu−Ni atomic ratio of 1:1, and the carbon layer with graphene structure was added on the surface to simulate the actual situation. As shown in Figure S4a, according to the XRD and XPS characterization results, Cu and Ni do not combine with carbon; they are connected with each other physically. Therefore, the model of physical interaction between the Cu−Ni alloy and the carbon layer is established and optimized. The active carbon sites corresponding to Cu and Ni in the CuNi@C alloy were labeled as I-type and II-type reaction pathways for DFT calculation, respectively (Figure S4b,c). The relevant parameters and information involved in DFT calculation are shown in Tables S1−S3.

The whole reaction consists of nine configurations, including seven local minima and two intermediate states (ISs) (Figure 4a). The reaction mechanism is given based on experimental results combined with previous work.[6] All calculated energy data are shown in Table S4, and NEB calculated energy data of intermediate states (ISs) are shown in Table S5 and Figure S5. Each state model can be found in Figures S6 and S7. The reaction is initiated by the adsorption of oxygen on the surface carbon. The adsorption relative energy of the II-type is −14.85 $kJ·mol^{-1}$, and that of the I-type is about +15.19 $kJ·mol^{-1}$. Relatively, the reaction is more easily initiated at the active site corresponding to Ni. However, since the lower energy barrier of the process can be completely overcome at room temperature, this does not mean that the copper site is difficult to react. Because of the rich charge of the Cu−Ni alloy and the good electron conduction of the graphite carbon layer, it is easy for oxygen to make electrons become superoxide species ($O_2^{\cdot-}$).[51] For the HCHO adsorption process of the two models, the energy of the system will be further reduced.

Then, induced by $O_2^{\cdot-}$, the C−H bonds in the HCHO molecule stretched and cleaved into ·OOH and HCO· species by coupling H· and O_2 (Figure 4b,d and Figure S6). This step has a higher activation energy (IS-1, $dE_{I\text{-}type}$ = 140.33 $kJ·mol^{-1}$, $dE_{II\text{-}type}$ = 130.62 $kJ·mol^{-1}$), but the energy changes of the first and last two states of the process are not obvious. Then, with the adsorption of water, the relative energy of the system further decreases. The dissociation of water is the rate-determining step of the reaction and has the highest activation energy in the reaction (IS-2, $dE_{I\text{-}type}$ = 249.41 $kJ·mol^{-1}$, $dE_{II\text{-}type}$ = 256.88 $kJ·mol^{-1}$) (Figure 4c−e and Figure S7). Water dissociation generates abundant surface hydroxyl groups, which accelerates the $HCHO/H_2O$ conversion reaction at the interface. Due to the highly active nature of HCO·, it tends to react with ·OH generated by water decomposition immediately to produce HCOOH. Then, the reaction ends up with H· and ·OOH forming H_2 and O_2. Figure 4a also shows that the relative energy of the II-type is relatively low in the whole reaction process, especially in the rate-determining step, i.e., water dissociation. DFT calculations reveal that the catalytic reaction is mainly carried out at the Cu active sites. The calculation of H_2 generation before HCOOH shows that the overall energy of the system is greatly increased, indicating that it is reasonable for HCOOH to be generated first (Figure S8).

3.4. Mechanism Discussion. To explore the participation of free radicals in the reaction, free-radical quenching experiments were carried out (Figure 5a). Under the same reaction conditions, 5 mL of furfural alcohol (FFA) and *tert*-butanol (TBA) were additionally added to the reaction system to quench ·HOO and ·OH. With the addition of a quenching agent, the H_2 generation rate in the reaction decreased significantly, confirming the existence of free radicals. Figure 5b is the EPR characterization for searching ·OH in the reaction. Different samples (20 mg) were added into the mixed aqueous solution of 0.8 M HCHO and 1 M KOH and stirred for 10 min to test the ·OH in the reaction. With the addition of a catalyst, the signal of ·OH appeared obviously in the solution. Cu@C has the highest free-radical signal, indicating that Cu@

https://doi.org/10.1021/acsami.1c11776
ACS Appl. Mater. Interfaces 2021, 13, 37299−37307

C has higher catalytic activity than Ni@C and $CN_{(1:1)}$. The performance of H_2 evolution of the sample is characterized by HER technology (Figure 5c). Obviously, the performance of Ni@C is better than those of Cu@C and $CN_{(1:1)}$, which indicates that nano-Ni has the best performance of H_2 evolution. The above experimental results show that the formation process of ·OH more likely occurs at Cu sites while the H_2 evolution reaction at Ni sites. Combined with the experimental results, the high catalytic HCHO dehydrogenation performance of $CN_{(1:1)}$ is mainly attributed to the synergistic effect of the high activity of nano-Cu and the high H_2 evolution performance of nano-Ni.

To sum up, combined with the experimental results and DFT calculations, the catalytic schematic of CuNi@C for H_2 generation in HCHO solution is obtained, as shown in Figure 5d. KOH was consumed by HCOOH produced during formaldehyde reforming, driving the reaction forward. The stoichiometric characteristics of the CuNi@C catalyst for dehydrogenation of HCHO are as follows:

$$HCHO + O_2 + H_2O$$

$$\rightarrow HCO\cdot + \cdot OOH + \cdot OH + \cdot H$$

$$\rightarrow HCOOH + \cdot OOH + \cdot H$$

$$\rightarrow HCOOH + O_2 + H_2$$

4. CONCLUSIONS

In summary, CuNi alloy−carbon layer core−shell nanoparticles have been prepared for efficient H_2 generation in HCHO solution. Physical characterizations prove the CuNi@C nanoparticles with a carbon shell and a CuNi alloy core, which is wrapped by a thin carbon layer. The CuNi@C nanoparticles with a Cu−Ni molar ratio of 1, i.e., $CN_{(1:1)}$, have the highest H_2 generation rate. The H_2 generation rate of the $CN_{(1:1)}$ is 110.98 $mmol \cdot g^{-1} \cdot h^{-1}$, which is 1.47 times and 4.93 times higher than those of Cu@C and Ni@C, respectively. According to the results of EPR, HER, and DFT calculations, the high activity of CuNi@C for efficient HCHO reforming into H_2 is based on two aspects. One is that the synergistic effect of the Cu and Ni metals in the CuNi@C alloy leads to a very high catalytic performance, in which Cu has a very high active species generation for HCHO decomposition and Ni has a very good H_2 evolution performance. The other is that the carbon layer of CuNi@C protects Cu and Ni from transition oxidation, which greatly enhances its stability. In this work, a stable and efficient catalyst for HCHO reforming into H_2 is developed at room temperature, making H_2 generation from industrial formaldehyde wastewater possible.

■ ASSOCIATED CONTENT

Supporting Information

The Supporting Information is available free of charge at https://pubs.acs.org/doi/10.1021/acsami.1c11776.

Additional characterization, influence of reaction conditions on the H_2 production rate, and relevant computational data (PDF)

■ AUTHOR INFORMATION

Corresponding Authors

Xin Cai − *Key Laboratory for Biobased Materials and Energy of Ministry of Education, College of Materials and Energy, South China Agricultural University, Guangzhou 510643, China;* orcid.org/0000-0002-2362-7776; Email: caixin2015@scau.edu.cn

Jihai Liao − *Department of Physics, South China University of Technology, Guangzhou 510640, China*; Email: jhliao@scut.edu.cn

Shengsen Zhang − *Key Laboratory for Biobased Materials and Energy of Ministry of Education, College of Materials and Energy, South China Agricultural University, Guangzhou 510643, China; Guangdong Laboratory for Lingnan Modern Agriculture, Guangzhou 510643 Guangdong, China;* orcid.org/0000-0002-6184-0201; Email: zhangss@scau.edu.cn

Authors

Zining Zhou − *Key Laboratory for Biobased Materials and Energy of Ministry of Education, College of Materials and Energy, South China Agricultural University, Guangzhou 510643, China*

Yun Hau Ng − *School of Energy and Environment, City University of Hong Kong, Hong Kong 999077, China;* orcid.org/0000-0001-9142-2126

Shengju Xu − *Key Laboratory for Biobased Materials and Energy of Ministry of Education, College of Materials and Energy, South China Agricultural University, Guangzhou 510643, China*

Siyuan Yang − *Key Laboratory for Biobased Materials and Energy of Ministry of Education, College of Materials and Energy, South China Agricultural University, Guangzhou 510643, China;* orcid.org/0000-0003-1210-1944

Qiongzhi Gao − *Key Laboratory for Biobased Materials and Energy of Ministry of Education, College of Materials and Energy, South China Agricultural University, Guangzhou 510643, China*

Yueping Fang − *Key Laboratory for Biobased Materials and Energy of Ministry of Education, College of Materials and Energy, South China Agricultural University, Guangzhou 510643, China; Guangdong Laboratory for Lingnan Modern Agriculture, Guangzhou 510643 Guangdong, China;* orcid.org/0000-0003-4311-6583

Complete contact information is available at: https://pubs.acs.org/10.1021/acsami.1c11776

Notes

The authors declare no competing financial interest.

■ ACKNOWLEDGMENTS

This research was supported by the National Natural Science Foundation of China (22078118, 21972048, and 21802046), the Guangdong Basic and Applied Basic Research Foundation (nos. 2021A1515010349, 2019A1515011138, and 2018A0303130018), and the Guangzhou Basic and Applied Basic Research Foundation (no. 202102080166).

■ REFERENCES

(1) Yang, H.; Cao, R.; Sun, P.; Yin, J.; Zhang, S.; Xu, X. Constructing Electrostatic Self-Assembled 2D/2D Ultra-Thin $ZnIn_2S_4$/Protonated g-C_3N_4 Heterojunctions for Excellent Photocatalytic Performance under Visible Light. *Appl. Catal., B* **2019**, *256*, 117862.

(2) Zheng, Y.; Xu, X. Surface Atom Regulation on Polyoxometalate Electrocatalyst for Simultaneous Low-Voltage H_2 Production and Phenol Degradation. *ACS. Appl. Mater. Interfaces* **2020**, *12*, 53739−53748.

(3) Lepage, T.; Kammoun, M.; Schmetz, Q.; Richel, A. Biomass-to-Hydrogen: A Review of Main Routes Production, Processes Evaluation and Techno-Economical Assessment. *Biomass Bioenergy* **2021**, *144*, 105920. (1-16).
(4) Chen, S.; Liang, S.; Wu, B.; Lan, Z.; Li, R. In Situ Generated Electron-Deficient Metallic Copper as the Catalytically Active Site for Enhanced Hydrogen Production from Alkaline Formaldehyde Solution. *ACS. Appl. Mater. Interfaces* **2019**, *11*, 33946−33954.
(5) Du, L.; Qian, K.; Zhu, X.; Yan, X.; Kobayashi, H.; Liu, Z.; Lou, Y.; Li, R. Interface Engineering of Palladium and Zinc Oxide Nanorods with Strong Metal−Support Interactions for Enhanced Hydrogen Production from Base-Free Formaldehyde Solution. *J. Mater. Chem. A* **2019**, *7*, 8855−8864.
(6) Liu, H.; Wang, M.; Ma, J.; Lu, G. Hydrogen Generation from Toxic Formaldehyde Catalyzed by Low-Cost Pd−Sn Alloys Driven by Visible Light. *J. Mater. Chem. A* **2020**, *8*, 9616−9628.
(7) Li, R.; Zhu, X.; Yan, X.; Kobayashi, H.; Yoshida, S.; Chen, W.; Du, L.; Qian, K.; Wu, B.; Zou, S. Oxygen-Controlled Hydrogen Evolution Reaction: Molecular Oxygen Promotes Hydrogen Production from Formaldehyde Solution Using Ag/MgO Nanocatalyst. *ACS Catal.* **2017**, *7*, 1478−1484.
(8) Fornari, A. M. D.; de Araujo, M. B.; Duarte, C. B.; Machado, G.; Teixeira, S. R.; Weibel, D. E. Photocatalytic Reforming of Aqueous Formaldehyde with Hydrogen Generation over TiO_2 Nanotubes Loaded with Pt or Au Nanoparticles. *Int. J. Hydrogen. Energy* **2016**, *41*, 11599−11607.
(9) Yan, X.; Duan, X.; Zhou, X.; Chen, S.; Liang, S.; Guo, Z.; Du, L.; Qian, K.; Zhu, X.; Li, R. The Interplay of Au Nanoparticles and ZnO Nanorods for Oxygen-Promoted, Base-Free, Complete Formaldehyde Reforming into H_2 and CO_2. *Catal. Commun.* **2018**, *117*, 5−8.
(10) Trincado, M.; Sinha, V.; Rodriguez-Lugo, R. E.; Pribanic, B.; de Bruin, B.; Grützmacher, H. Homogeneously Catalysed Conversion of Aqueous Formaldehyde to H_2 and Carbonate. *Nat. Commun.* **2017**, *8*, 1−11.
(11) Patra, S.; Singh, S. K. Hydrogen Production from Formic Acid and Formaldehyde over Ruthenium Catalysts in Water. *Inorg. Chem.* **2020**, *59*, 4234−4243.
(12) Wang, L.; Ertem, M. Z.; Kanega, R.; Murata, K.; Szalda, D. J.; Muckerman, J. T.; Fujita, E.; Himeda, Y. Additive-Free Ruthenium-Catalyzed Hydrogen Production from Aqueous Formaldehyde with High Efficiency and Selectivity. *ACS Catal.* **2018**, *8*, 8600−8605.
(13) Zou, Y.-Q.; von Wolff, N.; Anaby, A.; Xie, Y.; Milstein, D. Ethylene Glycol as An Efficient and Reversible Liquid-Organic Hydrogen Carrier. *Nat. Catal.* **2019**, *2*, 415−422.
(14) Li, R.; Li, Y.; Yang, P.; Wang, D.; Xu, H.; Wang, B.; Meng, F.; Zhang, J.; An, M. Electrodeposition: Synthesis of Advanced Transition Metal-Based Catalyst for Hydrogen Production Via Electrolysis of Water. *J. Energy Chem.* **2021**, *57*, 547−566.
(15) Liang, S.; Chen, S.; Guo, Z.; Lan, Z.; Kobayashi, H.; Yan, X.; Li, R. In Situ Generated Electron-Deficient Metallic Copper as the Catalytically Active Site for Enhanced Hydrogen Production from Alkaline Formaldehyde Solution. *Catal. Sci. Technol.* **2019**, *9*, 5292−5300.
(16) Bi, Y.; Lu, G. Nano-Cu Catalyze Hydrogen Production from Formaldehyde Solution at Room Temperature. *Int. J. Hydrogen. Energy* **2008**, *33*, 2225−2232.
(17) Chen, X.; Zhang, H.; Xia, Z.; Zhang, S.; Ma, Y. Base-Free Hydrogen Generation from Formaldehyde and Water Catalyzed by Copper Nanoparticles Embedded on Carbon Sheets. *Catal. Sci. Technol.* **2019**, *9*, 783−788.
(18) Preti, D.; Squarcialupi, S.; Fachinetti, G. Aerobic. Copper-Mediated Oxidation of Alkaline Formaldehyde to Fuel-Cell Grade Hydrogen and Formate: Mechanism and Applications. *Am. Ethnol.* **2009**, *121*, 4857−4860.
(19) Gao, H.; Zhang, J.; Wang, R.; Wang, M. Highly Efficient Hydrogen Production and Formaldehyde Degradation by Cu_2O Microcrystals. *Appl. Catal., B* **2015**, *172-173*, 1−6.
(20) Miao, L.; Nie, Q.; Wang, J.; Zhang, G.; Zhang, P. Ultrathin MnO_2 Nanosheets for Optimized Hydrogen Evolution Via Formaldehyde Reforming in Water at Room Temperature. *Appl. Catal., B* **2019**, *248*, 466−476.
(21) Jin, Q.; Shen, Y.; Cai, Y.; Chu, L.; Zeng, Y. Resource Utilization of Waste V_2O_5-Based deNO_x Catalysts for Hydrogen Production from Formaldehyde and Water Via Steam Reforming. *J. Hazard. Mater.* **2020**, *381*, 120934. (1-11).
(22) Qian, K.; Du, L.; Zhu, X.; Liang, S.; Chen, S.; Kobayashi, H.; Yan, X.; Xu, M.; Dai, Y.; Li, R. Directional Oxygen Activation by Oxygen-Vacancy-Rich WO_2 Nanorods for Superb Hydrogen Evolution Via Formaldehyde Reforming. *J. Mater. Chem. A* **2019**, *7*, 14592−14601.
(23) Ye, W.; Guo, X.; Ma, T. A Review on Electrochemical Synthesized Copper-Based Catalysts for Electrochemical Reduction of CO_2 to C^{2+} Products. *Chem. Eng. J.* **2021**, 128825. (1-16).
(24) Wu, M.; Zhu, C.; Wang, K.; Li, G.; Dong, X.; Song, Y.; Xue, J.; Chen, W.; Wei, W.; Sun, Y. Promotion of CO_2 Electrochemical Reduction Via Cu Nanodendrites. *ACS. Appl. Mater. Interfaces* **2020**, *12*, 11562−11569.
(25) Zhu, J.; Cheng, G.; Xiong, J.; Li, W.; Dou, S. Recent Advances in Cu-Based Cocatalysts toward Solar-to-Hydrogen Evolution: Categories and Roles. *Solar RRL.* **2019**, *3*, 1900256. (1-67).
(26) Li, N.; Yan, W.; Niu, Y.; Qu, S.; Zuo, P.; Bai, H.; Zhao, N. Photoinduced in Situ Spontaneous Formation of a Reduced Graphene Oxide-Enwrapped Cu−Cu_2O Nanocomposite for Solar Hydrogen Evolution. *ACS. Appl. Mater. Interfaces* **2021**, *13*, 9838−9845.
(27) Deka, P.; Borah, B. J.; Saikia, H.; Bharali, P. Cu-Based Nanoparticles as Emerging Environmental Catalysts. *Chem. Rec.* **2019**, *19*, 462−473.
(28) Santos, R. M. M.; Briois, V.; Martins, L.; Santilli, C. V. Insights into the Preparation of Copper Catalysts Supported on Layered Double Hydroxide Derived Mixed Oxides for Ethanol Dehydrogenation. *ACS. Appl. Mater. Interfaces* **2021**, *13*, 26001−26012.
(29) Chen, M.; Wang, H.; Chen, X.; Wang, F.; Qin, X.; Zhang, C.; He, H. High-Performance of Cu-TiO_2 for Photocatalytic Oxidation of Formaldehyde under Visible Light and the Mechanism Study. *Chem. Eng. J.* **2020**, *390*, 124481. (1-8).
(30) Zhang, F.; Chen, Z.; Fang, X.; Liu, H.; Liu, Y.; Zhu, W. Catalytic Activity of Cu/ZnO Catalysts Mediated by MgO Promoter in Hydrogenation of Methyl Acetate to Ethanol. *J. Energy Chem.* **2021**, *61*, 203−209.
(31) Mori, K.; Taga, T.; Yamashita, H. Synthesis of a Fe−Ni Alloy on a Ceria Support as a Noble-Metal-Free Catalyst for Hydrogen Production from Chemical Hydrogen Storage Materials. *ChemCatChem* **2015**, *7*, 1285−1291.
(32) Kang, W.; Guo, H.; Varma, A. Noble-Metal-Free NiCu/CeO_2 Catalysts for H_2 Generation from Hydrous Hydrazine. *Appl. Catal., B* **2019**, *249*, 54−62.
(33) Singh, S. K.; Singh, A. K.; Aranishi, K.; Xu, Q. Noble-Metal-Free Bimetallic Nanoparticle-Catalyzed Selective Hydrogen Generation from Hydrous Hydrazine for Chemical Hydrogen Storage. *J. Am. Chem. Soc.* **2011**, *133*, 19638−19641.
(34) Chen, S.; Liao, J.; Zhou, Z.; Yang, S.; Gao, Q.; Cai, X.; Peng, F.; Fang, Y.; Zhang, S. Boosting Photocatalytic Hydrogen Evolution Using a Noble-Metal-Free Co-Catalyst: CuNi@C with Oxygen-Containing Functional Groups. *Appl. Catal., B* **2021**, *291*, 120139.
(35) Löffler, T.; Meyer, H.; Savan, A.; Wilde, P.; Garzón Manjón, A.; Chen, Y.-T.; Ventosa, E.; Scheu, C.; Ludwig, A.; Schuhmann, W. Discovery of a Multinary Noble Metal−Free Oxygen Reduction Catalyst. *Adv. Energy Mater.* **2018**, *8*, 1802269. (1-7).
(36) Saha, S.; Ganguli, A. K. FeCoNi Alloy as Noble Metal-Free Electrocatalyst for Oxygen Evolution Reaction (OER). *ChemstrySelect* **2017**, *2*, 1630−1636.
(37) Cao, R.; Yang, H.; Zhang, S.; Xu, X. Engineering of Z-Scheme 2D/3D Architectures with $Ni(OH)_2$ on 3D Porous g-C_3N_4 for Efficiently Photocatalytic H_2 Evolution. *Appl. Catal., B* **2019**, *258*, 117997.
(38) Anjaneyulu, C.; Kumar, V. V.; Bhargava, S. K.; Venugopal, A. Characteristics of La-Modified Ni-Al_2O_3 and Ni-SiO_2 Catalysts for

https://doi.org/10.1021/acsami.1c11776
ACS Appl. Mater. Interfaces 2021, 13, 37299−37307

CO_x-Free Hydrogen Production by Catalytic Decomposition of Methane. *J. Energy Chem.* **2013**, *22*, 853−860.
(39) Chen, S.; Li, M.; Yang, S.; Li, X.; Zhang, S. Graphitied Carbon-Coated Bimetallic FeCu Nanoparticles as Original g-C_3N_4 Cocatalysts for Improving Photocatalystic Activity. *Appl. Surf. Sci.* **2019**, *492*, 571−578.
(40) Qi, W.; Liu, W.; Zhang, B.; Gu, X.; Guo, X.; Su, D. Oxidative Dehydrogenation on Nanocarbon: Identification and Quantification of Active Sites by Chemical Titration. *Angew. Chem. Int. Edit.* **2013**, *52*, 14224−14228.
(41) Zhang, J.; Liu, X.; Blume, R.; Zhang, A.; Schlögl, R.; Su, D. S. Surface-Modified Carbon Nanotubes Catalyze Oxidative Dehydrogenation of n-Butane. *Science* **2008**, *322*, 73−77.
(42) Zhang, P.; Zeng, G.; Song, T.; Huang, S.; Wang, T.; Zeng, H. Synthesis of a Plasmonic CuNi Bimetal Modified with Carbon Quantum Dots as a Non-Semiconductor-Driven Photocatalyst for Effective Water Splitting. *J. Catal.* **2019**, *369*, 267−275.
(43) Devaraj, M.; Saravanan, R.; Deivasigamani, R.; Gupta, V. K.; Gracia, F.; Jayadevan, S. Fabrication of Novel Shape Cu and Cu/Cu_2O Nanoparticles Modified Electrode for the Determination of Dopamine and Paracetamol. *J. Mol. Liq.* **2016**, *221*, 930−941.
(44) Zhao, X.; Abbas, S. C.; Huang, Y.; Lv, J.; Wu, M.; Wang, Y. Robust and Highly Active FeNi@NCNT Nanowire Arrays as Integrated Air Electrode for Flexible Solid-State Rechargeable Zn-Air Batteries. *Adv. Mater. Interfaces* **2018**, *5*, 1701448. (1-7).
(45) Wen, Y.; Liu, Y.; Dang, S.; Tian, S.; Li, H.; Wang, Z.; He, D.; Wu, Z.-S.; Cao, G.; Peng, S. High Mass Loading Ni-Decorated Co_9S_8 with Enhanced Electrochemical Performance for Flexible Quasi-Solid-State Asymmetric Supercapacitors. *J. Power Sources* **2019**, *423*, 106−114.
(46) Zhu, J.; Chen, J.; Luo, Y.; Sun, S.; Qin, L.; Xu, H.; Zhang, P.; Zhang, W.; Tian, W.; Sun, Z. Lithiophilic Metallic Nitrides Modified Nickel Foam by Plasma for Stable Lithium Metal Anode. *Energy. Storage. Mater.* **2019**, *23*, 539−546.
(47) Huang, B.; Bartholomew, C. H.; Woodfield, B. F. Improved Calculations of Pore Size Distribution for Relatively Large, Irregular Slit-Shaped Mesopore Structure. *Microporous Mesoporous Mater.* **2014**, *184*, 112−121.
(48) Zhang, S.; Li, M.; Zhao, J.; Wang, H.; Zhu, X.; Han, J.; Liu, X. Plasmonic AuPd-Based Mott-Schottky Photocatalyst for Synergistically Enhanced Hydrogen Evolution from Formic Acid and Aldehyde. *Appl. Catal., B* **2019**, *252*, 24−32.
(49) Suenobu, T.; Isaka, Y.; Shibata, S.; Fukuzumi, S. Catalytic Hydrogen Production from Paraformaldehyde and Water Using an Organoiridium Complex. *Chem. Commun.* **2015**, *51*, 1670−1672.
(50) Liu, H.; Wang, M.; Zhang, X.; Ma, J.; Lu, G. High Efficient Photocatalytic Hydrogen Evolution from Formaldehyde over Sensitized Ag@Ag-Pd Alloy Catalyst under Visible Light Irradiation. *Appl. Catal., B* **2018**, *237*, 563−573.
(51) Tang, C.; Zhang, Q. Nanocarbon for Oxygen Reduction Electrocatalysis: Dopants, Edges, and Defects. *Adv. Mater.* **2017**, *29*, 1604103. (1-9).

https://doi.org/10.1021/acsami.1c11776
ACS Appl. Mater. Interfaces 2021, 13, 37299−37307